Journal of ELECTRONIC MATERIALS, Vol. 44, No. 11, 2015
DOI: 10.1007/s11664-015-3953-8

Investigation of the Physical Properties of Sprayed Nanocrystalline In_2S_3 Films

N. BOUGUILA,[1,6] M. KRAINI,[1] I. NAJEH,[1] I. HALIDOU,[2] E. LACAZE,[3] H. BOUCHRIHA,[4] H. BOUZOUITA,[5] and S. ALAYA[1]

1.—Laboratoire de Physique des Matériaux et des Nanomatériaux appliquée à l'environnement, Faculté des Sciences de Gabès, Université de Gabès, Cité Erriadh, Zrig, 6072 Gabès, Tunisia. 2.—Département de Physique, Faculté des Sciences et Techniques, Université Abdou Moumouni, BP 10662, Niamey, Niger. 3.—CNRS, UMR7588, Institut des NanoSciences de Paris (INSP), 4 place Jussieu, 75005 Paris, France. 4.—LPMC, Faculté des Sciences de Tunis, Le Belvédère, 1060 Tunis, Tunisia. 5.—Laboratoire de Photovoltaïque et Matériaux Semi-conducteurs, Ecole Nationale des Ingénieurs de Tunis, Belvédère, BP 37, 1002 Tunis, Tunisia. 6.—e-mail: bouguila.nour@gmail.com

In_2S_3 films have been grown on preheated glass substrate by spray pyrolysis. Indium chloride and thiourea in the molar ratio S:In = 2 were used as reagents. Substrate temperature was fixed at 613 K. These films adhered well to the substrate and were approximately 2 μm thick. Structural, morphological, optical, and electrical properties of the as-grown In_2S_3 films were studied by use of x-ray diffraction (XRD) analysis, energy-dispersive spectroscopy, atomic force microscopy (AFM), optical absorption spectroscopy, and impedance spectroscopy. XRD revealed well crystallized films oriented in the (400) direction corresponding to the cubic β-In_2S_3 phase. The surface of the films was smooth; average roughness was 5 nm. The AFM image revealed that the films were nanopolycrystalline and contained grains in the range 20–30 nm. Optical transmission in the visible and near-infrared regions was 80%. The direct band-gap energy was 2.62 eV. The electrical data were analyzed on the basis of the impedance Cole–Cole plots in the frequency range 0.1 Hz to 100 kHz at room temperature. Constant-phase elements were used in equivalent electrical circuits for fitting of experimental impedance data. The experimental results were fitted to the equivalent electrical circuit by use of Z-view software. The conductivity of grains and grain boundaries was estimated. The gas-sensing properties of the sample were investigated on the basis of the change in conductance as a result of adsorption and desorption of atmospheric oxygen.

Key words: Spray pyrolysis, In_2S_3 thin films, XRD, AFM, hopping conduction, gas sensor

INTRODUCTION

Interest in indium sulfide (In_2S_3) has increased during the last 10 years because of its high potential for many applications. This material is an important semiconductor with a band gap varying from 2 to 3.5 eV, depending on chemical composition and deposition conditions.[1–3] In_2S_3 is a good candidate for replacing the toxic material CdS in thin-film chalcogenide-based solar cells. It can also be used as a catalyst and a luminophore, and in buffer layers, electrodes, and gas sensors, because of its catalytic, optical, electronic, and gas-sensing properties.[4–14] In_2S_3 can also be used for fabrication of oxygen gas sensors, because of the dependence of its conductance on oxygen adsorption and desorption. Oxygen gas sensors are widely used in medical, environmental, and domestic applications.[15–17] Among the materials used for this purpose, semiconducting metal oxides have attracted most attention in the past few years. The mechanism of sensing of such

(Received April 28, 2015; accepted July 21, 2015; published online August 14, 2015)

gas sensors is based on surface reaction, and the microstructure of the material is one of the most important factors affecting sensitivity.[18] In addition, to enhance sensitivity and achieve lower operating temperatures, noble metals are added. However, these types of sensor still suffer from such problems as long-term stability and high operating temperature.[19] Few studies have been devoted to the gas-sensing properties of In_2S_3. In_2S_3 usually crystallizes with the tetragonal structure and occurs as several crystalline phases, for example α, β, γ and ε, depending on preparation conditions.[14] Among these phases, β-In_2S_3 is the most stable at room temperature. In_2S_3 films have been prepared by several methods. Spray pyrolysis is one of the most convenient, because of its simplicity and low cost; it is also highly suitable for deposition on large-area substrates.

In the work discussed in this paper, we investigated the properties of In_2S_3 for oxygen gas sensing at room temperature. Films were prepared by spray pyrolysis. The effect of oxygen pressure on the electrical properties of the films was studied by impedence spectroscopy. We showed that this wide-gap material can be used for fabrication of competitive oxygen gas sensors operating at room temperature. The mechanism of oxygen detection is discussed.

EXPERIMENTAL

In_2S_3 films were prepared on glass substrates by use of spray pyrolysis of a solution containing thiourea $SC(NH_2)_2$ and indium chloride $InCl_3$ as sources of S^{2-} and In^{3+}, respectively. The molar ratio of S to In in the solution was 2. The solution and gas flow rates were kept constant at 2 L min^{-1} and 6 L min^{-1}, respectively. Compressed nitrogen was used as carrier gas. During the growth, the substrate temperature was fixed at 613 K. To avoid oxidation the films were cooled to approximately 473 K under nitrogen flow before removal from the hotplate.

Film thickness was measured by use of a Talystep profilometer. A clearly distinguishable step is apparent in Fig. 1. The film thickness was approximately 2 μm, so the corresponding average rate of deposition was approximately 0.1 μm/min.

The structures of the layers were characterized by use of an x-ray diffractometer (Philips PW 1729) with CuKα monochromatic radiation (λ = 1.5406 Å). Morphological characterization was performed by atomic force microscopy (Digital Instruments Nanoscope II). A.c. electrical investigations were conducted with an impedance analyzer (HPLF 4192A). For electrical characterization, two gold electrodes were evaporated in planar geometry. The conductivity of the In_2S_3 films was determined by use of impedance spectroscopy.

RESULTS AND DISCUSSION

X-ray Diffraction and EDS Analysis

The x-ray diffraction (XRD) pattern of an In_2S_3 film deposited at a substrate temperature of T_s = 613 K is depicted in Fig. 2. The four peaks are related to (311), (400), (511), and (440) of cubic β-In_2S_3, according to JCPDS card no. 65-0459. The (400) peak is the most prominent, indicating that this orientation is preferred. We thus inferred that grains grew predominantly along the (400) plane as a result of lower interfacial energy. That all the XRD peaks are indexed to the In_2S_3 cubic phase is an indication of the crystallographic purity of the samples. No characteristic peaks were observed for such impurities as In_2O_3, S or $In(OH)_3$. The XRD main peak values expected for these impurities according to JCPDS cards nos. 71-2194, 76-2242, and 76-1464 are In_2O_3 (2θ = 30.586°), S (2θ = 23.093°), and $In(OH)_3$ (2θ = 22.279°), respectively. The average grain size of the film, calculated by use of Scherrer's equation, was approximately 30 nm.

The atomic percentages of In and S were determined by energy-dispersive spectroscopy (EDS) measurements on different points of the film surface

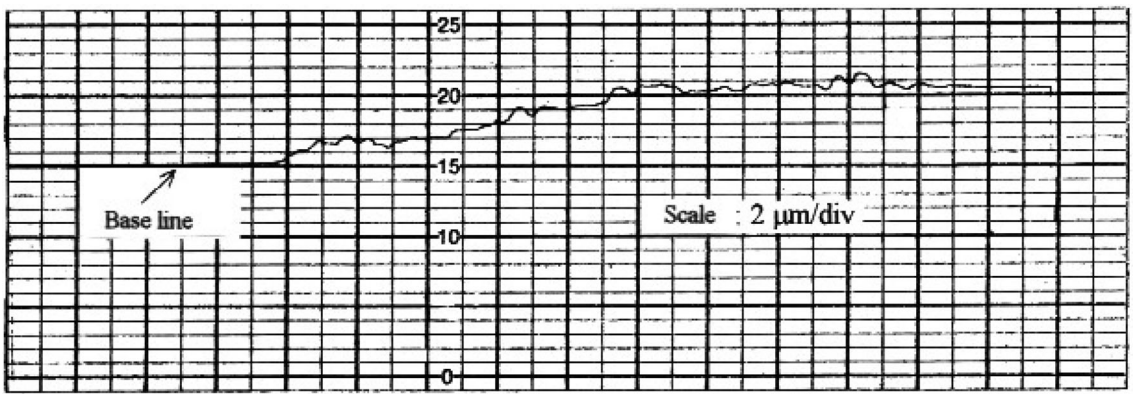

Fig. 1. Talystep profile of In_2S_3 film.

to verify its homogeneity. The measured EDS spectra were almost identical, meaning our film was homogeneous. A typical EDS spectrum of the film is presented in Fig. 3. It is clearly apparent that the main chemical components of the film are indium and sulfur. However, other chemical elements, for example oxygen, silicon, and aluminum were also detected, but in much smaller amounts. We believe they are related to the glass substrate, because these elements are the main components of commercial glass, and EDS probes a depth of up to 3 μm. The Cl atoms probably arise from unreacted precursors.[16] The average S:In atomic ratio is approximately 1.2. This is slightly less than the stoichiometric ratio (1.5) and can be explained by evaporation of sulfur, even at low temperatures.

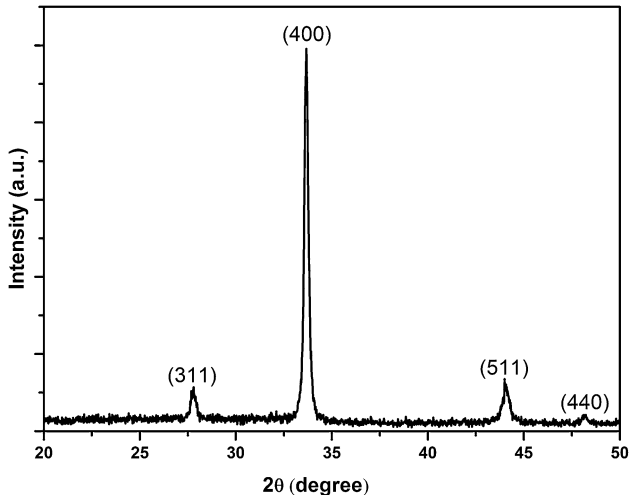

Fig. 2. XRD spectrum of In_2S_3 film.

AFM Analysis

Surface topography was studied by use of atomic force microscopy. Figure 4 shows a two dimensional atomic force microscopy (AFM) image of the In_2S_3 layer, scanned over an area of 1 μm × 1 μm. The polycrystalline structure of the film is clearly apparent. Indeed, it can be seen that the surface is formed by crystallites with diameters of approximately 250 nm which probably correspond to column tops in the microstructure.[20] These crystallites are separated by depressions and consist of grains, as shown in Fig. 5. The average grain size of the film varied in the range 20–30 nm. This value confirms the XRD results. Fig. 4b shows the roughness profile of the film surface along the direction marked in Fig. 4a. The average surface roughness is in the order of 5 nm. A similar value was reported by W. Vallejo et al.[4] on In_2S_3 co-evaporated films deposited on glass substrates. While the profile depicted in Fig. 5b reveals the local roughness of a crystallite along the direction marked on the AFM image (Fig. 5a). The crystallite surface is flat with a local roughness of 1.5 nm. Gas-sensitive properties are strongly correlated with the microstructure of the films and can be modified by changing the surface-to-volume ratio of the grains.

Optical Properties

The optical transmittance and reflectance spectra of In_2S_3 film prepared at T_s = 613 K are shown in Fig. 6. A sharp UV cut-off is observed at approximately 370 nm. The transmission coefficient is more than 80% and the reflection coefficient is approximately 20%. The large-amplitude of the interference fringes is indicative of high reflectance, and there is little scattering or absorption in the bulk of the film.[21]

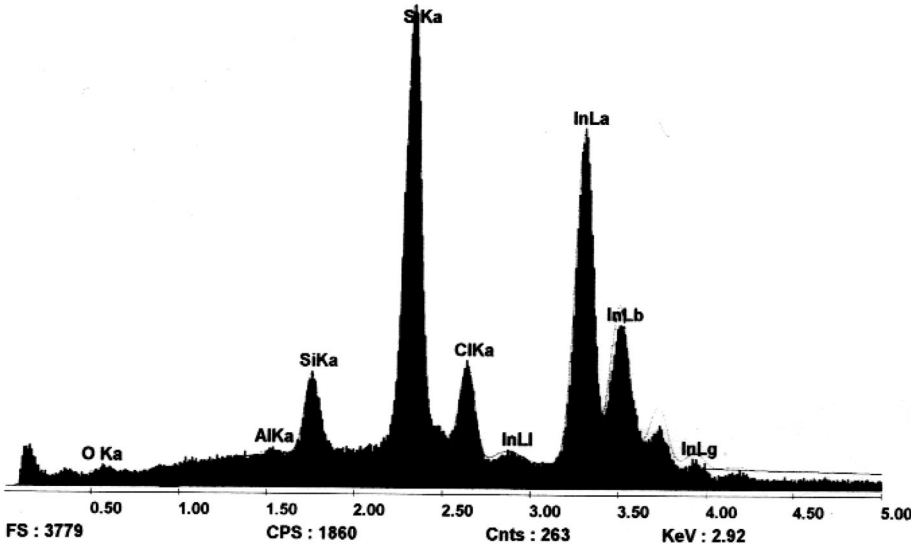

Fig. 3. EDS spectrum of In_2S_3 film.

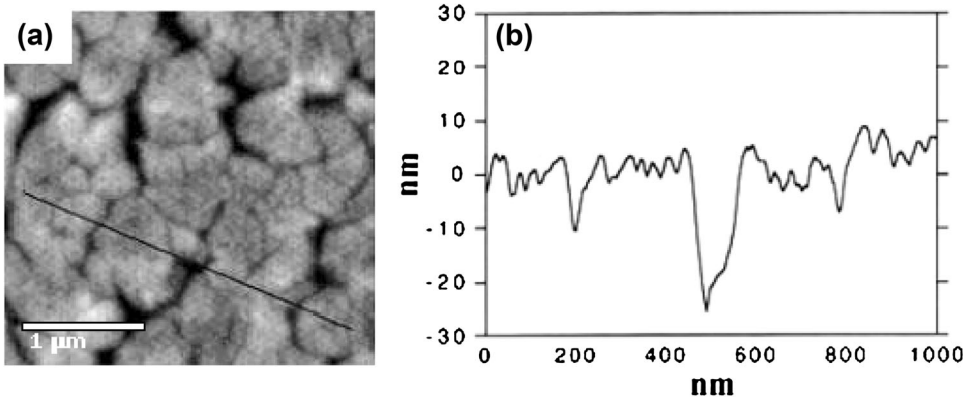

Fig. 4. (a) AFM topography of the surface of In_2S_3 film and (b) roughness surface profile along the direction marked in (a).

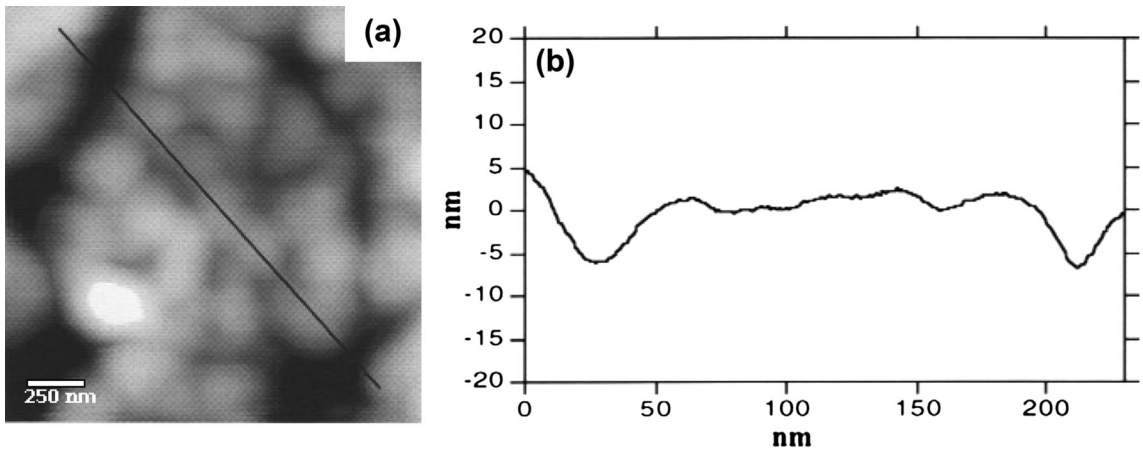

Fig. 5. (a) AFM topography of a single crystallite and (b) roughness surface profile along the direction marked in (a).

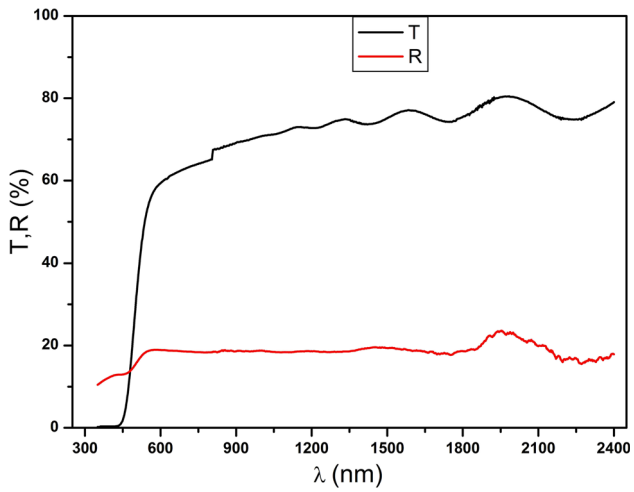

Fig. 6. Optical transmission and reflectance spectra of In_2S_3 film.

Values of the absorption coefficient at the fundamental absorption edge were calculated from the transmittance and reflectance data by use of the formula:

$$T = (1 - R)e^{-\alpha d}, \tag{1}$$

where R is the reflectance, α the absorption coefficient, and d the thickness of the sample.

The optical band gap (E_g) of the film was determined from the variation of the absorption coefficient (α) as a function of photon energy ($h\nu$). The optical band-gap energy was determined by use of the relationship:

$$(\alpha h\nu) = A(h\nu - E_g)^{\frac{1}{2}}, \tag{2}$$

where A is a constant which depends on the probability of transition. A plot of $(\alpha h\nu)^2$ as a function of $h\nu$ is shown in Fig. 7. The band-gap energy can be determined by extrapolating the linear portion of the curve to the photon energy axis. The band gap was found to be 2.62 eV. This value is similar to those reported for In_2S_3 thin films prepared by flash evaporation, the SILAR method, and chemical spray pyrolysis.[22–24] The deviation from the gap value of the single In_2S_3 crystal (~2 eV) may be because of the quantification effect induced by the nanocrystalline structure of the films. The wide band gap of In_2S_3 films is favorable for gas-sensing applications.

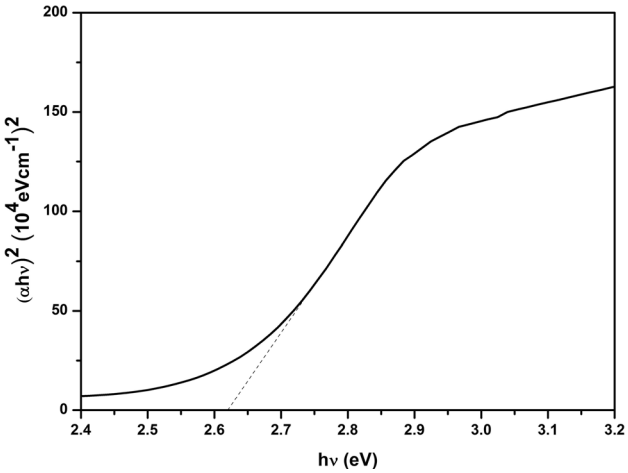

Fig. 7. A plot of $(\alpha h\nu)^2$ as a function of photon energy ($h\nu$) for In_2S_3 film.

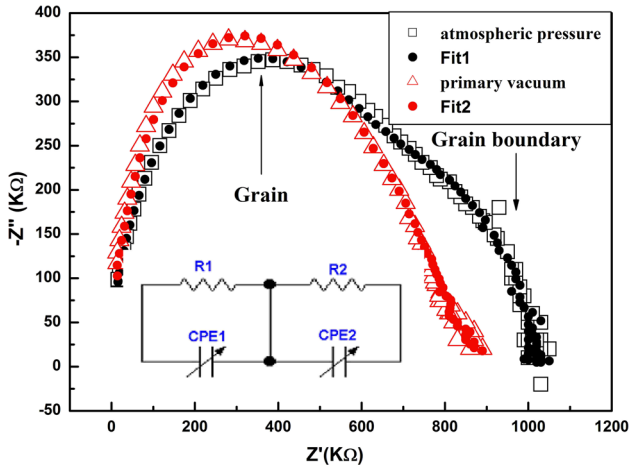

Fig. 8. Complex Impedance plots at 300 K, and the equivalent circuit used to represent the electrical properties of grain and grain boundary effects.

Impedance Spectroscopic Analysis

The impedance behavior of the In_2S_3 nanoparticles at 300 K is depicted in Fig. 8.

This figure shows the relationship between the real (Z') and imaginary (Z'') parts of the complex impedance, which form two arcs. Modeling of the impedance semicircles by use of Z-view software reveals that they comprise a pair of parallel resistances and capacitances connected in series. The experimental impedance data can be analyzed by means of impedance spectroscopy. In this instance the ideal equivalent circuit must be modified by introducing constant-phase elements (CPE) to substitute for C. It is known that the impedance of a CPE can be described by $Z_{\mathrm{CPE}} = \frac{1}{C(j\omega)^{\alpha}}$. The complex impedance of a single parallel R–CPE is given by:[25,26]

$$Z = \frac{R}{1 + RC(j\omega)^{\alpha}} \tag{3}$$

For $\alpha = 0$ the CPE behaves as an ideal resistor and when $\alpha = 1$ the CPE behaves as an ideal capacitor. Experimentally, α is found to be between 0 and 1.

In the equivalent circuit two CPEs replace both capacitive components, C_1 corresponding to grains and C_2 to the grain boundary regions. The impedance, corresponding to this equivalent circuit, takes the form:[27]

$$Z = \frac{R_1}{1 + R_1C_1(j\omega)^{\alpha_1}} + \frac{R_2}{1 + R_2C_2(j\omega)^{\alpha_2}}. \tag{4}$$

This following equivalent circuit was used for data fitting by use of commercial software (Z-view). In the fitting procedure, first, it is necessary to take the starting values R_1 and R_2 for each component in the circuit and, then, to find the most appropriate values. The fitted values used for the circuit are presented in Table I. Although the equivalent circuit contains a large number of fitting terms (six), all are allowed to vary simultaneously by in-house software based on the Simplex method. Satisfactory fitting of data, with different α values, indicates that the dependence of capacitance on frequency is different in intensity for grains and grain-boundary regions. We believe that CPE1 and CPE2 elements with $\alpha_1 \geq 0.90$ of In_2S_3 correspond mainly to capacitors, whereas CPE1 with $\alpha_2 = 0.80$ corresponds both to the resistive and capacitive behavior of the bulk region. The results shown in Fig. 8 illustrate the validity of the proposed equivalent circuit and results from successful application of the in-house software that enables assessment of the most plausible model.

Electrical Conduction

The ac conductance was calculated from measured impedance over the frequency range 0.1 Hz to 100 kHz by use of the formula:[28]

$$G(\omega) = \frac{Z'}{Z'^2 + Z''^2}, \tag{5}$$

where $G(\omega)$ is the conductance of the In_2S_3 sample.

The dependence of measured conductivity on frequency is shown in Fig. 9.

A frequency-independent plateau in the low-frequency region changes to a monotonous increase with frequency in the high-frequency region (>10 Hz). This behavior obeys the universal power law:[29,30]

$$G(\omega) = G_{\mathrm{dc}} + A\omega^{s}, \tag{6}$$

where G_{dc} is the dc conductance (frequency-independent plateau in the low frequency region), A is the pre-exponential factor, and s is the fractional exponent between 0 and 1, corresponding to a hop-

Table I. Values of equivalent circuit term deduced from experimental data fits

Terms	R_1 (Ω)	C_1 (nF)	α_1	R_2 (Ω)	C_2 (nF)	α_2	τ_1 (s)	τ_2 (s)	R_T (Ω)
Atmospheric pressure	566,840	19	1.016	446,880	412	0.83	0.01123	0.1050	1013,720
Primary vacuum	702,300	16.26	1.014	157,420	1586	0.81	0.01215	0.1803	859,720

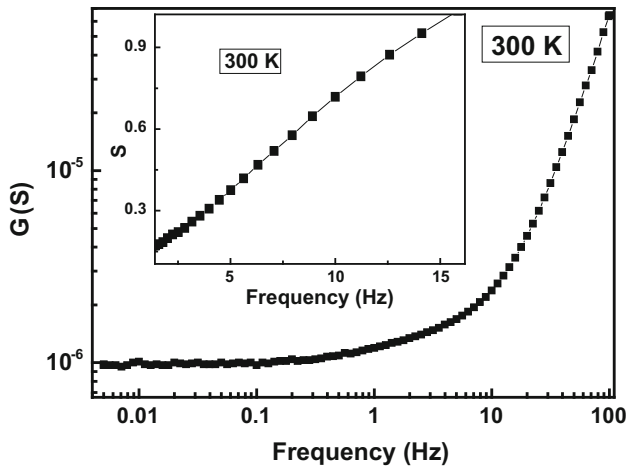

Fig. 9. Ac conductivity as a function of frequency. Inset: frequency dependence of the exponent s for In_2S_3 at 300 K.

ping process. Therefore, charge carrier transport could occur by hopping between the localized states, which can be explained by Mott's hopping model.[31] Some of the trap states, created by disordered atoms and incomplete bonding between them, could be filled by the carriers depending on their distribution in the band gap. The empty states may capture electrons from the charged states and hence conduction would be followed by hopping of charge carriers from filled trap states to empty trap states.[32]

The dc conductivity is frequency-independent, i.e. $G = G_{dc} = 10^{-6}\ \Omega^{-1}$.

According to the results in Table I, the contribution of both grain boundary resistance and grain resistance to the total resistance of the film is: $R = R_1 + R_2 = 1.02 \times 10^6\ \Omega$, i.e.:

$$\frac{1}{G} = \frac{1}{G_1} + \frac{1}{G_2}, \tag{7}$$

where $G \leftarrow (1/R)\psi$ is total conductance, reverse of R, G_1 is grain conductance, and G_2 grain boundary conductance. Thus, the total conductance is the result of parallel association of the conductance of the grains and the boundary of the grains. For a polycrystalline material the total impedance Z_T can be written as:[33] $Z_T = R_1 + R_2 = Z_g + Z_{gb}$ where Z_g and Z_{gb} are the complex impedance contribution of the grains and grain boundaries contacts, respectively. Each can be represented as a resistance (R) and capacitance (C) in parallel.

The power exponent s is given by:

$$s = \frac{d \ln \sigma_{ac}(\omega)}{d \ln \omega}. \tag{8}$$

The frequency-dependence of the exponent s is calculated from $\log G_{ac}$–$\log f$ plots. The variation of s with frequency, shown in the inset of Fig. 9, gives useful information about the specific conduction mechanism involved. As is clearly apparent from this figure, s is frequency-dependent; in fact, s increases with increasing frequency. s is <1, which corresponds to a long-distance hopping process. However, s increases with increasing frequency at T = 300 K. Thus, in the correlated barrier-hopping (CBH) model, s increases with increasing frequency similar to the experimental data obtained at T = 300 K. The frequency exponent in the CBH model is given by the equation:[34]

$$s(\omega, T) = 1 - \frac{6kT}{W_m + kTLn(\omega\tau_{oh})}, \tag{9}$$

where W_m is the energy required to remove an electron from one site (activation energy), and τ_{oh} is the relaxation time. Using the best fit to experimental data, one can calculate W_m = 300 meV and $\tau_{oh} = 10^{-13}$ s at T = 300 K. This result is compatible with the assumption of electronic hopping between localized sites.[35,36]

The different films were placed in a vacuum test chamber, the chamber was evacuated (10^{-3} Torr), then air was introduced. As is apparent from Table I, the resistance Z_T decreases in a vacuum.

It is well known that In_2S_3 is an n-type wide band-gap semiconductor with excess sulfur vacancies acting as donors. During exposure of the film to air, molecular oxygen acts as an electron acceptor, reducing the number of electrons in the conduction band of the In_2S_3 semiconductor. Oxygen in the form O_2^-, O^- or O^{2-}, depending on temperature, is chemisorbed on the material surface and on the grain boundaries.[37] The reaction between oxygen molecule and the surface of the samples can be described by the equation:

$$e^- + \frac{1}{2}O_2(g) \leftrightarrow O_2^-, \text{ at temperatures } < 100^\circ\text{C}. \tag{10}$$

The incorporated ions result in a surface Schottky barrier build up of an electron-depleted region in the material, which leads to the increase in resistance. During the pumping phase, however, the film loses the adsorbed oxygen. The ionic oxygen is des-

orbed from the film as molecular oxygen (O_2), leaving one or two electrons per atom. The electrons are then re-introduced to the conduction band, leading to a decrease of resistance[18] because of lowering of the potential barrier at the grain boundary and the increase of the carrier density.

CONCLUSION

By use of a spray technique we deposited In_2S_3 films on glass substrate maintained at 613 K. Film thickness was approximately 2 μm. XRD studies revealed that the In_2S_3 films grew along the preferred (400) orientation in the cubic β-In_2S_3 phase without any secondary phases. AFM measurements indicated that the films were nanopolycrystalline in structure and consisted of 20–30 nm grains. Local and average surface roughness were 1.5 nm and 5 nm, respectively. Optical analysis revealed that the film was of high quality with high transparency (>80%). The absorption coefficient was 4×10^4 cm^{-1} in the transmission region. The band-gap energy was 2.62 eV. Impedance analysis and circuit Modeling for complex impedance plots resulted in two equivalent (R–CPE) parallel circuits for grains and grain boundaries. Higher frequency response with larger resistance was attributed to grain effects. Relaxation times were different for charge carrier transport originating from grains and from grain boundaries. Agreement between experimental and simulated results was good. The circuit variable (α), ≥0.85 at 300 K, reveals the capacitive nature of the bulk and the grain boundaries. The fractional exponent s was between 0 and 1, corresponding to a hopping process. Values of s increased with increasing frequency at T = 300 K, similar to the behavior of the CBH model. Because of their electrical conductance change in different atmospheres, In_2S_3 films are promising materials for oxygen gas sensor applications at room temperature.

ACKNOWLEDGEMENTS

The authors would like to thank Pr A. Belhadj Amara (Faculté des Sciences de Bizerte, Tunisie) and Pr Z. Fakhfakh (Faculté des Sciences de Sfax, Tunisie) for XRD and EDS measurements, respectively. The authors are also grateful to H. Rahmouni (Institut Supérieur des Sciences appliquées et de Technologie de Kasserine, Tunisie) for manuscript revision and useful discussions.

REFERENCES

1. N. Barreau, S. Marsillac, D. Albertini, and J.C. Bernède, *Thin Solid Films* 403–404, 331 (2002).
2. E.B. Yousfi, T. Asikainen, V. Pietu, P. Cowache, M. Powalla, and D. Lincot, *Thin Solid Films* 183, 361 (2000).
3. N. Barreau, J.C. Bernède, and S. Marsillac, *J. Cryst. Growth* 241, 51 (2002).
4. I. Puspitasari, T.P. Gujar, K.D. Jung, and O.S. Joo, *J. Mater. Process. Technol.* 201, 775 (2008).
5. W. Vallejo and J. Clavijo, *Braz. J. Phys.* 40, 30 (2010).
6. A. Datta, S. Gorai, D. Ganguli, and S. Chaudhuri, *Mater. Chem. Phys.* 102, 195 (2007).
7. S. Gorai and S. Chaudhuri, *Mater. Chem. Phys.* 89, 332 (2005).
8. A. Datta, S.K. Panda, D. Ganguli, P. Mishra, and S. Chaudhuri, *Cryst. Growth Des.* 7, 163 (2007).
9. S. Yu, L. Shu, Y. Qian, Y. Xie, and J. Yang, *Mater. Res. Bull.* 33, 717 (1998).
10. X. Chen, Z. Zhang, X. Zhang, J. Liu, and Y. Qian, *Chem. Phys. Lett.* 407, 482 (2005).
11. J. Yang, C. Lin, Z. Wang, and J. Lin, *Inorg. Chem.* 45, 8973 (2006).
12. L.Y. Chen, Z.D. Zhang, and W.Z. Wang, *J. Phys. Chem. C* 112, 4117 (2008).
13. Y. Liu, H. Xu, and Y. Qian, *Cryst. Growth Des.* 6, 1304 (2006).
14. N. Bouguila, H. Bouzouita, E. Lacaze, A.B. Amara, H. Bouchriha, and A. Dhouib, *J. Phys. III Fr.* 7, 1647 (1997).
15. J. Watson, *Sens. Actuators* 5, 29 (1984).
16. E.F. Schipper, R.P.H. Kooyman, R.G. Heidman, and J. Greve, *Sens. Actuators B* 24–25, 90 (1995).
17. A.D. Brailsford and E.M. Logothetis, *Sens. Actuators B* 52, 195 (1998).
18. J.H. Yu and G.M. Choi, *Sens. Actuators B* 52, 251 (1998).
19. W.P. Kang and C.K. Kim, *Appl. Phys. Lett.* 63, 421 (1993).
20. D. Le Bellac, G.A. Niklasson, and C.G. Granqvist, *Europhys. Lett.* 32, 155 (1995).
21. J. George, K.S. Joseph, B. Pradeep, and T.I. Palson, *Phys. Status Solidi (a)* 106, 123 (1988).
22. K. Bouabid, A. Ihlal, A. Outzourhit, and E.L. Ameziane, *Act. Passiv. Electron. Compon.* 27, 207 (2004).
23. H.M. Pathan, C.D. Lokhande, S.S. Kulkarni, D.P. Amalnerkar, T. Seth, and S.H. Han, *Mater. Res. Bull.* 40, 1018 (2005).
24. S. Elfarrass, B. Hartiti, A. Ridah, and P. Thevenin, *J. Mater. Environ. Sci.* 6, 487 (2015).
25. E. Şentürk, *J. Sol. State Chem.* 177, 1508 (2004).
26. S. Komornicki, M. Radecka, and M. Rekas, *J. Mater. Sci.* 12, 11 (2001).
27. J.H. Park and B.C. Choi, *J. Cryst. Growth* 276, 465 (2005).
28. M. Vijayakumar, P. Muralidharan, M. Venkateswarlu, and N. Satyanarayana, *Mater. Chem. Phys.* 95, 16 (2006).
29. A.K. Jonscher, *Dielectric Relaxation in Solids* (London: Chelsea Dielectric Press, 1983).
30. A.K. Jonscher, *Nature* 267, 673 (1977).
31. N. Revathi, P. Prathap, Y.P.V. Subbaiah, and K.T.R. Reddy, *J. Phys. D Appl. Phys.* 41, 155404 (2008).
32. D.K. Paul and S.S. Mitra, *Phys. Rev.* 34, 1000 (1973).
33. P. Knauth and J. Schoonman, *Nanostructured Materials* (Dordrecht: Kluwer Academic Publishers, 2002), p. 111.
34. G.F. Pike, *Rev. B* 6, 1572 (1972).
35. A. Oberlin, G. Terriere, and J.L. Boulmier, *Tanso* 83, 153 (1975).
36. A. Oberlin, G. Terriere, and J.L. Boulmier, *Tanso* 80, 29 (1975).
37. D.H. Yoon and G.M. Choi, *Sensor. Actuators B* 45, 251 (1997).